A Scanning Tunneling Microscopy Study of Monolayer and Bilayer Transition-Metal Dichalcogenides Grown by Molecular-Beam Epitaxy

Maohai Xie and Jinglei Chen

Physics Department, The University of Hong Kong, Pokfulam Road, Hong Kong

Abstract:

This review presents an account of some recent scanning tunneling microscopy and spectroscopy (STM/S) studies of monolayer and bilayer transition-metal dichalcogenide (TMD) films grown by molecular-beam epitaxy (MBE). In addition to some intrinsic properties revealed by STM/S, defects such as inversion domain boundaries and point defects, their properties and induced effects, are presented. More specifically, the quantum confinement and moiré potential effects, charge state transition, quasi-particle interference and structural phase transition as revealed by STM/S are described.

1. Introduction

Recent interests in monolayer (ML) transition-metal dichalocogenides (TMDs), such as molybdenum or tungsten disulfides and diselenides (MoS_2, WS_2, $MoSe_2$, and WSe_2), stem from their attractive electronic and optoelectronic properties, including order-of-magnitude increase in photoluminescence intensity [1,2], large exciton binding energy [3-11], novel spin and valley contrasted physics [12-17], etc. ML-TMDs also hold the promise for future two dimensional (2D) nano-sized devices with enhanced performances and/or new functionalities [18]. Initially, most of the experimental works on ML-TMDs were carried out on exfoliated or chemical vapor deposition (CVD) grown samples [19-22]. Lately, efforts by molecular-beam epitaxy (MBE) are increasingly made, which has led to new discoveries using *in situ* surface characterization techniques such as scanning tunneling microscopy and spectroscopy (STM/S) [23-32]. In this review, a brief account of some recent STM/S studies of epitaxial $MoSe_2$, WSe_2 and $MoTe_2$ is presented. An emphasis is placed on defects and their associated properties and effects. The paper is organized as follows: in section 2, a discussion on STM contrast is presented, which is followed in section 3 by a discussion of some intrinsic properties of ML and bilayer (BL) $MoSe_2$ and WSe_2 as revealed by STM/S measurements.

Section 4 introduces inversion domain boundary (IDB) defects commonly seen in epitaxial molybdenum dichalcogenides (*i.e.*, $MoSe_2$ and $MoTe_2$), their properties as affected by quantum confinement and the moiré superlattice potentials. Section 5 concerns about point defects, their charge state transition and the induction of quasi-particle interference (QPI). In section 6, a study of phase tuning of epitaxial $MoTe_2$ is presented. Finally, in section 7 a summary and conclusion is given.

2. STM contrast

The most commonly studied TMD MLs consist of a close-packed metal (Mo or W) layer sandwiched between two layers of similarly close-packed chalcogen atoms (S, Se or Te) that are arranged in the trigonal prismatic (2H) or distorted octahedral (1T') configuration. The 2H phase TMDs are typically semiconductors whereas the 1T' phase TMD ML usually shows the metallic behavior. Bulk crystals of TMDs are made of stacks of MX_2 (M = Mo or W, X = S, Se, or Te) ML units held via the weak van der Waals (vdW) forces. Because of the latter, ML TMD can be obtained readily by exfoliation [19].

The ease of preparing clean surfaces of TMDs by cleaving bulk crystals made them among the first materials being studied by STM [33,34]. It was recognized then that the large contributions from the *d*-orbitals of the transition-metal atoms at Fermi level would make STM image interpretation ambiguous. The large accessibility in energy of these states could be balanced by the large spatial separation between the subsurface layer of the metal atoms and the STM tip, so the bright contrast in STM images might be associated with either the metal or chalcogen atoms depending on imaging conditions. By a study of $Mo_xW_{1-x}Se_2$ alloy, it was concluded that the subsurface transition-metal layer had a large influence on empty-state imaging whereas the topmost chalcogen atom layer would contribute more to the filled state STM images [34]. This may be understood by the fact that in multilayer thick TMDs (*e.g.*, $MoSe_2$), the conduction band minimum (CBM) at the K-point of the Brillouin zone (BZ) is dominated by the d_{z^2} orbital of the transition-metal whereas states at the valence band maximum (VBM) at the BZ center (Γ-point) has a reduced d_{z^2} contribution but an increased p_z-orbital contribution from chalcogen atoms [35]. Therefore the empty-state image would be dominated by the metal atoms whereas the filled-state image could be more related to chalcogen atoms. In the case of ML TMDs, however, metal contribution from the $d_{x^2-y^2}$ and

d_{xy} orbitals to the VBM state, which now locates at the BZ corner (K-point), is much more enhanced [36]. So STM contrast can be different from that of bulk crystals.

Figures 1a and **1b** show respectively an empty and filled state STM image of the same area of an epitaxial $MoSe_2$ ML grown by MBE on highly oriented pyrolytic graphite (HOPG) substrate. Ignoring the wagon-wheel like features, which will be discussed later, one notes clearly the difference in shape and position of the bright spots in the two images. To illustrate this, we overlay in the two images line and circles highlighting the spatially shifted or aligned rows of atoms when a wagon-wheel 'spoke' is crossed. Note that in the empty-state image, *atom* rows are shifted, whereas in the filled-state image no such misalignment is observed upon crossing a wagon-wheel spoke. Knowing that the latter represents a Se-cored twin domain boundary (see section 4 below), it can be assigned that the bright spots in the two STM images reflect different atoms – one for metal (a) and the other for Se (b), in an apparent agreement with the above discussions about the STM contrast of a bulk TMD. However as mentioned, ML TMD is different from multi-layer films and the VBM located at the BZ corners (the K-points) has greater metal contributions. Looking at the shape of the bright spots in Figs. 1(a) and 1(b), one may note that it is triangular for the empty state image but circular for the filled state image. This difference in shape is in odd with the shapes of the d orbitals of the metal atoms at the CBM and VBM. On the other hand, for surface chalcogen (Se) atoms, the $p_{x,y}$ orbitals have substantial contributions to the conduction band, which may better explain the spot shape in Fig. 1(a). We would nevertheless like to remark that the two images shown in Fig. 1(a) and 1(b) were taken at energies slightly away from the CBM and VBM, which may have a different weighting in contribution from different atomic orbitals to the overall density-of-states (DOS).

With the above general comment made, we wish to also point out that the very feature of the STM contrast of $MoSe_2$ is sensitively dependent on the STM tip conditions. This is best illustrated in **Figure 1c**, where upon an accidental tip change during scanning, the STM contrast changed correspondingly from the empty-state like on top to the filled-state like at the bottom, despite that the bias condition was not changed in the experiment. Hence, there is not a simple and universal assignment about the origin of the STM contrast of TMDs.

3. Intrinsic Properties of TMDs as Revealed by STM/S Studies

Epitaxial $MoSe_2$ was firstly attempted in the 90's of the last century by MBE growth where MoS_2 or SnS_2 was used as the substrate. The interaction between the epilayer and the substrate was of the weak vdW force, which ensured a strain-free epifilm to be grown and yet the specific aligned epitaxial relation was observed. The latter feature characterizes the so called vdW-epitaxy [37-39] and has been applied to growth of some other layered materials as well [40-42]. With the current interests in 2D materials, vdW epitaxy of TMDs for ML thickness rejuvenated and a great progress has been made both in the understanding of the growth processes and in improving the quality of the vdW epilayers. New phenomena and properties are discovered from epitaxial TMD ML or few-layers through in situ STM/S studies.

Figure 2a presents a topographic image of an epitaxial WSe_2 deposited on HOPG by MBE for a nominal coverage of 1.4 MLs, where the kinetics dictates that both monolayer and bilayer thick films coexisted on the same sample but otherwise atomically flat and clean terraces as shown by the atomic resolution image in the inset. A similar morphology was found for epitaxial $MoSe_2$ though the latter usually contained high density of inversion domain boundary defects to be discussed in detail in the next section. STS measurements of such a sample in both the ML and BL regions reveal semiconducting behavior showing the DOS gaps (**Figure 2b**). Specifically, for ML WSe_2, the band gap is found to be 2.59 eV and that for BL WSe_2 it is 1.83 eV [32]. Similarly for ML and BL $MoSe_2$, the electronic gaps are determined to be 2.25 eV and 1.72 eV, respectively, by STS measurements [32].

There is, however, an ambiguity in assigning the band edges from the measured STS data. In the above, we have followed the method of Ref. [25] by plotting the differential conductance spectra in the logarithm scale and the band edges were then determined by the intersections of the zero-conductance 'floor' in the spectra with the linear fits of the conductance data in regions close to the band edges [32]. For the case of ML $MoSe_2$, complication arises due to the fact that both the conduction and valence band edges are located at the K point of the BZ (for monolayer WSe_2, the CBM is located at Q point, about mid-way between Γ and K in the BZ) with a large parallel momentum $\mathbf{k}_{\parallel}$ and thus a high tunneling decay constant $\kappa = \sqrt{\frac{2m\Phi + k_{\parallel}^2}{\hbar^2}}$, where Φ is the energy barrier for tunneling [43,44]. As a result, states at the band edge are not sensitively picked up by STM measurements and can be missed out from the STS data. By acquiring the $\left(\frac{\partial Z}{\partial V}\right)_I$ spectrum, where Z is the sample

and STM-tip separation, Zhang et al. identified the true edges of the energy bands that were closer to Fermi level [23]. Therefore, the energy gaps of monolayer $MoSe_2$ and WSe_2 should be slightly less than the above quoted values.

Accurate determination of electronic gaps is crucial in assessing the exciton binding energies in TMD MLs, an issue of great fundamental and practical importance [3-11,25]. Indeed, due to the diminishing effect of screening in low-dimensional systems, high exciton binding energy is expected. In photoluminescence (PL) experiments of the TMD MLs, the strong PL peak reflects excitonic transitions. By comparing the PL peak energy with the electronic gap derived from STS, one may derive directly the binding energy of excitons [25]. We followed such an approach to have similarly derived the exciton binding energies of 0.72 eV and 0.59 eV in ML WSe_2 and $MoSe_2$, respectively [32].

Another interesting observation is made by examining the STS spectra taken in the vicinity of a step separating ML and BL TMD terraces. **Figures 3a** and **3b** show an example for WSe_2 and **Figure 3c** schematically summarizes the findings. Firstly, a band offset is revealed which amounts to 0.37 eV for the valence band and 0.19 eV at the conduction band. The difference in band offsets between the valence and conduction band edges reflects relative strength of coupling of states at the two bands. Indeed, density functional theory (DFT) calculations revealed that states at the CBM of WSe_2 (the Q-point) have greater Se *p*-orbital ($p_{x,y}$) contributions and a moderate coupling of these states will leads to a down-shift in energy in the BL films. The VBM of ML WSe_2, on the other hand, occurs at BZ boundary (K point) that is mainly of the *d*-orbital of the metal and thus suffers little from interlayer coupling. Instead, states at the BZ center having significant contribution from Se p_z-orbitals will couple strongly, leading to a much greater up-shift of the Γ band [36]. Therefore, while the conduction band minimum (Q valley) down shifts a little by interlayer coupling of the $p_{x,y}$ orbitals of the Se atoms, the valence band maximum shifts from the K to the up-shifted Γ states. This is clear from **Figures 3d** and **3e**, the DFT calculated band structures for monolayer and bilayer WSe_2 [32]. The second interesting feature noted from Figs. 3a-3c is an apparent upward band-bending at both sides of the step. Similar observation was made also in Ref. [24]. This is unusual, which can however be explained by an effect of Fermi level pinning. In other words, it may indicate the presence of mid-gap states at the step, which could be also indicated by the enhanced contrast in STM images of TMD ML islands and/or clusters (**Figure 3f**) [30,45]. The as-grown WSe_2 are nearly intrinsic away from steps for both

the ML and BL domains, so Fermi level pinning naturally leads to the homogeneous upward band bending at two sides of the step.

4. Inversion Domain Boundaries in MBE-Grown $MoSe_2$ and 2H-$MoTe_2$

As early as in the 90's of the last century when researchers examined the surfaces of MBE-grown $MoSe_2$ epifilms on SnS_2 and MoS_2, some regularly arranged line structures were noted in the STM images [37,39,46]. The periodicity of the superstructures was found to closely match that of the moiré pattern due to the lattice misfits between $MoSe_2$ and the substrate and so those line features were assigned as the moiré interference effect [37,39]. In 2014 when we experimented growth of ML $MoSe_2$ on HOPG or graphene/SiC, similar line features were discovered [27]. The period, which was found to be in the range of 4 – 6 nm, was however found inconsistent with the expected moiré periodicity of the system (~ 1 nm). Surprisingly, similar line features were observed even in $MoSe_2$ grown on Au(110) substrate having very different lattice symmetry and lattice constants. So we assigned that they were not moiré patterns.

Figure 4a shows an example of the line-decorated $MoSe_2$ surface grown on HOPG by MBE. The bright lines are seen to intertwine, giving rise to the triangle network or the 'wagon-wheel' structure on surface. **Figure 4b** is a close-up image showing the fine details of the lines or 'spokes' of the wagon-wheels. These bright lines are not caused by the geometric height difference but reflect locally enhanced DOS, since their contrast showed an apparent bias dependence during STM imaging. From Figure 4b, one further notes that each spoke is composed of two closely spaced and mirror-symmetric lines, along which the intensities undulate along their lengths.

By combining transmission electron microscopy (TEM) and DFT studies, the origin of these line features was identified as inversion domain boundaries abundant in epitaxial $MoSe_2$ [27,29,30,47,48]. By some recent high-resolution annular dark field scanning TEM (STEM) imaging, it was unambiguously established that the IDBs are Se-cored mirror twin boundaries and thus represents a chalcogen-deficient structure in $MoSe_2$ [47-50]. **Figures 5a** and **5b** show a STEM image and corresponding stick-and-ball model of the IDB in $MoSe_2$ ML [50]. The formation of such defects can be attributed to a state that accommodates Se vacancies in $MoSe_2$ epifilms [29,32,47].

Another and perhaps a more striking feature seen in Figure 4b is the intensity undulations along the lengths of the IDBs. The cause of such intensity undulation is still under debate. Firstly, it may reflect the quantum well state (QWS) due to the finite length of each IDB as intersected by crossing other defects in the network. The intersection junctions acted as the scatters for electron waves running along the defect, giving rise to a standing wave and thus undulated intensity. Such quantum confinement effect may be evidenced from the energy-dependent undulation period (**Figure 6a**) derivable from STS maps such as that shown in **Figures 6b** and **6c**. It shows clearly a dispersion relation and for a given defect of fixed length, one notes a relation of $\lambda/\lambda' = n/(n+1)$, where n is an integer, λ and λ' are the wavelengths (undulation period) at two different energies, affirming the QWS. Besides such energy-dependent undulation periods, one also observes undulations of a fixed period of ~ 1 nm over wider energy ranges (*e.g.*, the groups of data circled in Fig. 6a). Recognizing that the 1 nm period matches that of the moiré pattern in the system, we invoked an effect of Bragg reflection due to the superlattice potential of the moiré patterns along defect to explain such energy independent undulation wavelength [27]. In other words, there is effectively a band-folding effect and thus standing waves corresponding to the moiré periodicity. The assignment that the moiré superlattice potential causes the Bragg reflection in ML $MoSe_2$ may be supported by the observation that, unlike in ML $MoSe_2$, undulations of shorter wavelengths exist in BL $MoSe_2$. For the latter, the moiré potential may have become significantly weakened for the top layer electrons and so there is no more Bragg reflection [29]. Recently, another mechanism was suggested to explain such an intensity undulation, *i.e.*, a charge density wave (CDW) caused by Peierls instability for one-dimensional metallic systems at Fermi level E_F [47]. Examining the STS of Figure 6a measured at 4 K, one indeed notes an apparent gap at the Fermi level, which amounts to as much as ~ 210 meV. This gap is however much larger than that reported in Ref. [47] (73 meV) and if it were the CDW gap, it would translate a CDW phase transition at a higher temperature. A recent transport experiment did suggest a CDW transition at the temperature of ~ 227 K [48]. On the other hand, verification by a varying-temperature STM will be highly desirable.

There thus appear to be at least three possible causes for the observed intensity undulations in STM/S along the IDB: (i) quantum confinement effect that give rise to the energy-dependent (dispersive) undulation period; (ii) moiré superlattice potential induced Bragg reflection and/or (iii) Peierls instability induced CDW causing the undulations of the fixed period of ~ 1 nm. Bragg reflection can be responsible for those fixed-period undulations recorded at energies far from the Fermi energy (*e.g.*, the data group '1' in Fig. 6a), while

CDW could be that for the data in group '2' and '3'. More experiments are still called for to distinguish and verify these different factors.

Finally, we note that a similar IDB network is also observed in epitaxial 2H-phase $MoTe_2$ as exemplified in **Figure 7a**. However, in $MoTe_2$ it has a much higher density (~ 2 nm in length) than that in $MoSe_2$ prepared under similar growth conditions. Interestingly, no such IDB network is found in MBE-grown WSe_2, nor in films prepared by other methods like CVD. Another feature seen in Fig. 7a is that with shrinking triangle domain size delineated by the IDB network, the STM images of $MoTe_2$ show a non-uniform or an undulated contrast that is dependent both on the domain size and on the bias condition of the STM (*cf*. **Figures 7b** and **7c**, **7d**) [31]. This phenomenon can be attributed to the quantum dot states confined in the small triangle domains, akin to that in an isolated triangular TMD island as revealed by a theoretical study [51].

5. Charge State Transition and Quasi-Particle Interference Induced by Point Defects

In addition to line defects, there are also abundant point defects, such as isolated Se or metal vacancies, adatoms and interstitials. Such vacancy or adatom defects would behave like donors or acceptors in the semiconductor host, whose charge state transition due to a STM tip-induced electric field can be captured by STM/S imaging [29]. **Figure 8a** shows an example of a STS map of a $MoSe_2$ BL, in which a bright elliptical ring as highlighted by the red line is discerned. It arises from an ionization of a point defect close to the STM tip as it scans the sample, where the electric field exerted by the tip causes a band-bending and when the defect energy level E_D crosses the Fermi level E_F, transition of the charge state of the defect occurs, giving rise to an enhancement of tunneling current and thus the STS contrast [52-55]. Changing the bias of the tip changes the relative lateral position where E_D intersects with E_F and thus the size of ionization rings. **Figure 8b** presents a cut of the ionization ring at different energies, revealing the variation of the ring size with energy. The parabolic shape signals a donor defect. Simulation of the parabola assuming an effective dielectric constant of BL $MoSe_2$ to be 4.6 results in a binding energy of the defect of ~ 0.24 eV, or else knowing the energy of the defect, one derives the dielectric constant of the film [29]. The dielectric property can be of particular interest for 2D systems, which is the cause of many fascinating properties such as large exciton binding energy as described earlier. Therefore, STM may provide a convenient means to study such properties.

Another effect that a defect can bring is the induced quasi-particle scattering readily captured by STM/S. In $MoSe_2$ and WSe_2 MLs, electron and hole are in two inequivalent valleys separated by a large crystal momentum. A localized defect can facilitate scattering of the charged particles between different valleys. **Figure 9a** shows a STS map taken in the vicinity of the point defect in an epitaxial WSe_2 ML and at the energy close to the CBM. **Figure 9b** is a Fourier transform of the STS map revealing a quasi-particle interference (QPI) pattern [28]. By comparing with the calculated joint density of states at the corresponding energy (**Figure 9d**), we assert that this QPI reflects the spin-conserving inter-Q valley scattering of conduction electrons as indicated by the green arrows in **Figure 9c,** a constant energy contour map. Spin-conserving inter-valley scattering signifies long valley and spin lifetime in ML WSe_2, which is a key figure of merit for spin and valley electronic applications.

6. Phase Tuning of $MoTe_2$ during MBE Growth

$MoSe_2$ and WSe_2 have the stable hexagonal structure and are direct-gap semiconductors for monolayer thick films. On the other hand, $MoTe_2$ exists in two different phases – 2H or 1T', where the latter is semi-metallic and draws increasing attention lately due to some attractive properties like huge magnetoresistance [56-62], topological insulator [63-65] and Weyl semimetal states [66-70]. The large difference between electrical properties of its 2H versus 1T' phase of $MoTe_2$ also makes it attractive for phase-change electronics. Therefore, control and tuning of the phases of epitaxial $MoTe_2$ can be of great scientific and practical importance. We employ MBE to grow $MoTe_2$ ML on HOPG and obtained both 2H and 1T' phases with varying compositions. The topographic STM image of an as-grown $MoTe_2$ is shown in **Figure 10a**. It reveals monolayer islands but with both 2H and 1T' phases over the film. **Figures 10b** presents an atomic-resolution STM image of a 2H-$MoTe_2$ ML while **Figures 10c** is for a 1T'-$MoTe_2$ domain [31]. From the latter high resolution STM micrographs, one sees the distinct hexagonal and rectangular symmetries of the two phases. As described before, abundant IDBs are present in as-grown $MoTe_2$ forming the dense triangular network, whereas in 1T' film, few extended defects can be discerned.

It is often that in an as-grown film both 2H and 1T' phases exist as revealed by STM and also by reflection-high energy electron diffraction (RHEED). **Figure 11a** shows an example of the RHEED patterns taken during $MoTe_2$ deposition on HOPG, in which diffraction streaks from the substrate, 2H- and 1T'-$MoTe_2$ are all discernable as marked by the colored

arrows. The relative intensities of the 1T' and 2H streaks are plotted in **Figures 11b and 11c** for growth at different temperatures and different Te fluxes, respectively. They reveal a degree of tenability of the structural phases of epitaxial $MoTe_2$ [31]. Furthermore, by a post-growth annealing procedure, we could achieve a pure 2H-phase $MoTe_2$, although it remains challenging to obtain a pure 1T'-$MoTe_2$ epilayer. By consultation with the DFT calculations, we attribute the phase change to an effect of Te surface adsorption where high adsorbate coverage favors $1T'$-phase $MoTe_2$ nucleation and growth [31].

In the 1T'-domain, we often observe intensity 'bands' in the STS maps that run parallel to the a-axis of the crystal. An example is shown in **Figure 12a** where quasi-periodic bright bands vertical in the image are clearly seen. Fast Fourier transform of such STS images reveals extra intensity spots at distances $\Delta k \sim 0.55$ Å^{-1} from the center but along the $\Gamma - Y$ direction of the BZ (see **Figure 12b**). According to theory, a freestanding 1T'-$MoTe_2$ ML has electron valleys along $\Gamma - Y$, which is $0.28 \sim 0.32$ Å^{-1} from the BZ center [31]. **Figure 12c** presents a constant-energy contour map illustrating such electron valleys. Therefore, an inter-valley scattering (marked by the arrow) would generate standing waves of wave-vectors $0.56 \sim 0.64$ Å^{-1} that closely matches that of the experiment. In other words, the intensity bands seen in Figure 10a are likely quasi-particle interference patterns, which may be induced by domain boundaries or edges abundant in the film.

7. Summary and conclusions

In summary, by employing STM/S, we have revealed a number of interesting phenomena and properties of epitaxial $MoSe_2$, WSe_2 and $MoTe_2$ MLs or BLs grown by MBE. In addition to the intrinsic properties such as fundamental gaps, extrinsic properties such as line and point defects and their induced effects are studied. For the intensity undulations seen along the line defects, quantum confinement, Bragg reflection and Peierls instability are all invoked to interpret the phenomenon. For point defects, tip-induced ionization and an inter-valley scattering are discovered. The latter holds great fundamental and practical importance as they reflect implicitly the strength of screening in ultrathin layers and the lifetime of spin and valley degree of freedom. Finally, we reveal an effect of phase tuning of epitaxial $MoTe_2$ by changing the MBE conditions or annealing, which can be associated with the effect of Te adsorption on the surface of a growing film.

Acknowledgement

Many people are involved in the work described in this review. In particular, Drs. H.J. Liu and L. Jiao contributed the growth experiments by MBE, F. Yang, G.Y. Wang, H. Zheng, C.L. Gao and J.F. Jia helped the low-temperature STM/S measurements. H.Y. Yu, W. Yao, and X.Q. Dai provided various theoretical supports. We are also very grateful to J.H. Hong and C.H. Jin for sharing with us the STEM result of Figure 5. Finally, we acknowledge the financial support from a Collaborative Research Grant (C7036-17W) as well as a General Research Fund (17327316) of the Research Grant Council of Hong Kong Special Administrative Region, China.

Figures and Captions:

Figure 1 (a) An empty-state STM image (size: 14×14 nm^2, bias: 1.09 V) of an as-grown $MoSe_2$ ML on HOPG. (b) A filled-state STM image (size: 14×14 nm^2, bias: -1.70 V) of the same area as in (a). In both, the white circles mark the bright dots in the images which are laterally shifted in (a) but aligned in (b) upon crossing a line defect. (c) A STM image (size: 18×18 nm^2, bias: 1.21 V), showing the change of STM contrast upon an accidental change of the tip condition. Reprinted (c) with permission from ref. [27]. Copyright (2014) by the American Physical Society.

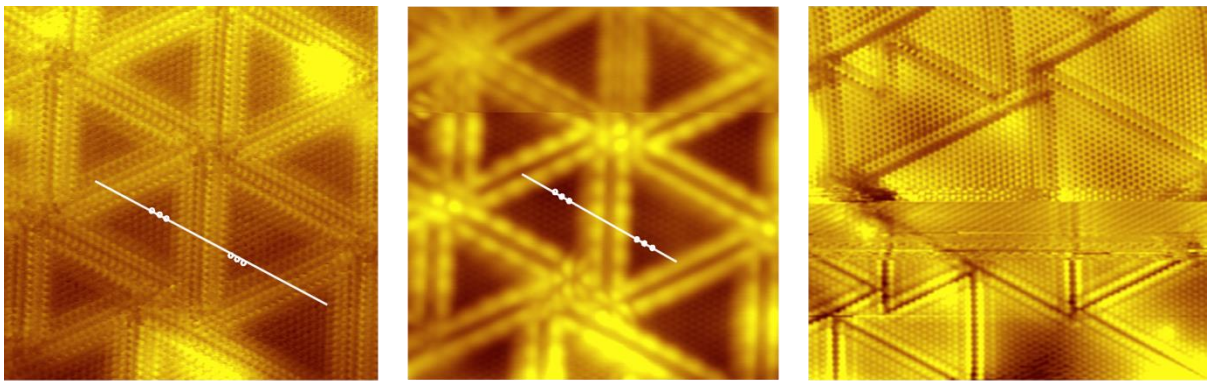

(a) (b) (c)

Figure 2 (a) A STM micrograph (size: 75×75 nm^2, bias: 2.4V) of a MBE-grown WSe_2 on HOPG, in which monolayer (ML), bilayer (BL) and trilayer (TL) domains/islands coexist as marked. Inset: atomic resolution STM image (size: 7.5×7.5 nm^2, bias: 0.8V) of the ML domain showing a clean surface and the moiré pattern. (b) STS of both ML (black) and BL (green) WSe_2 domains. Each curve represents an average of 50 measurements [28,32].

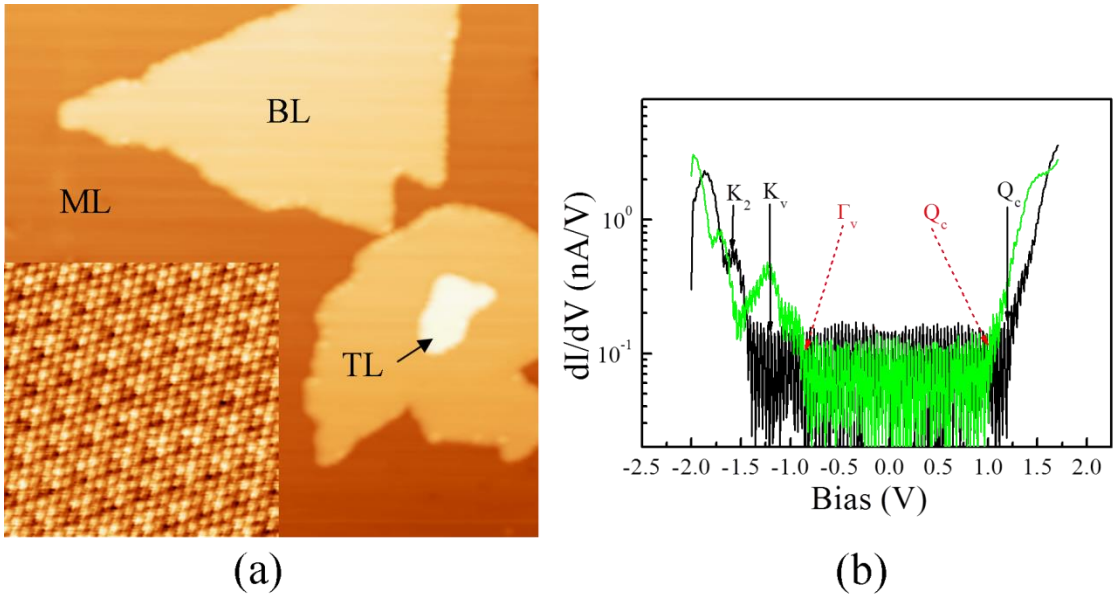

(a) (b)

Figure 3 STS of (a) ML and (b) BL WSe_2 in the vicinity of a ML-high step. (c) Schematic diagram illustrating the band offset and band bending. (d, e) Electronic band structures of (d) ML and (e) BL WSe_2 calculated by the DFT. (f) A STM image (size: 250×250 nm^2, bias: 0.5V) showing enhanced STM contrast at the edges/steps [32].

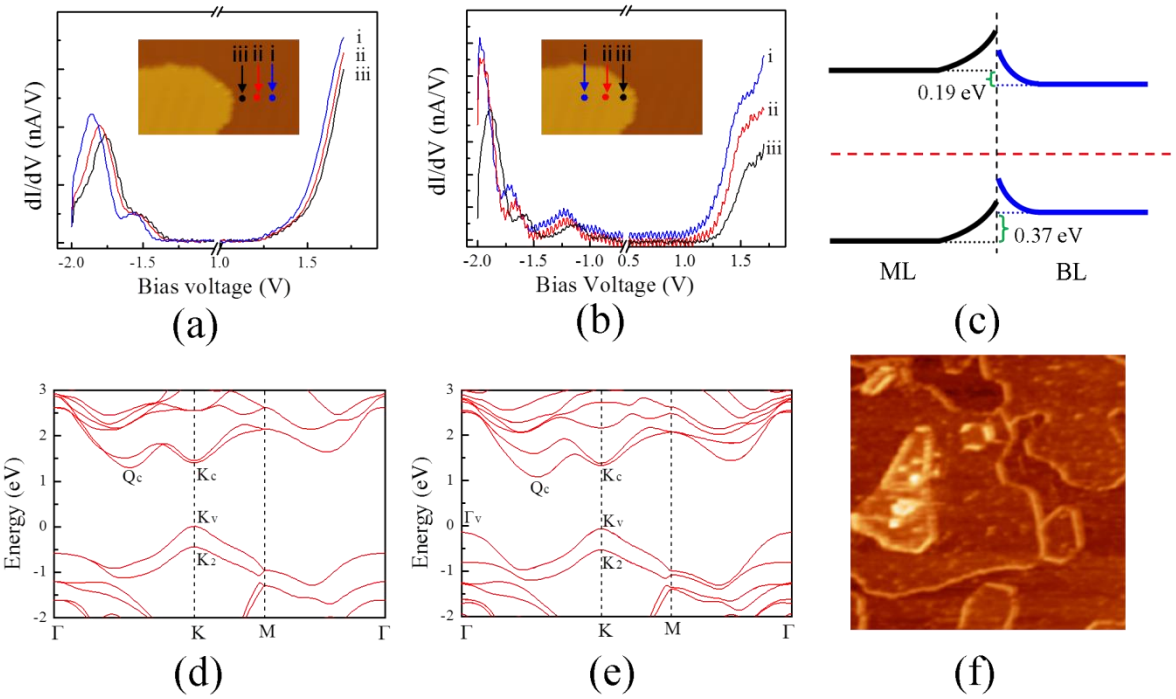

Figure 4 (a) STM topographic image (size: 50×50 nm^2, bias: -1V) of an as-grown $MoSe_2$ of 1.4 MLs coverage on HOPG. (b) A close-up STM image (size: 13×13 nm^2, bias: -1.46V) revealing intensity undulations along the line defects. Reprinted with permission from Ref. [27]. Copyright (2014) by the American Physical Society.

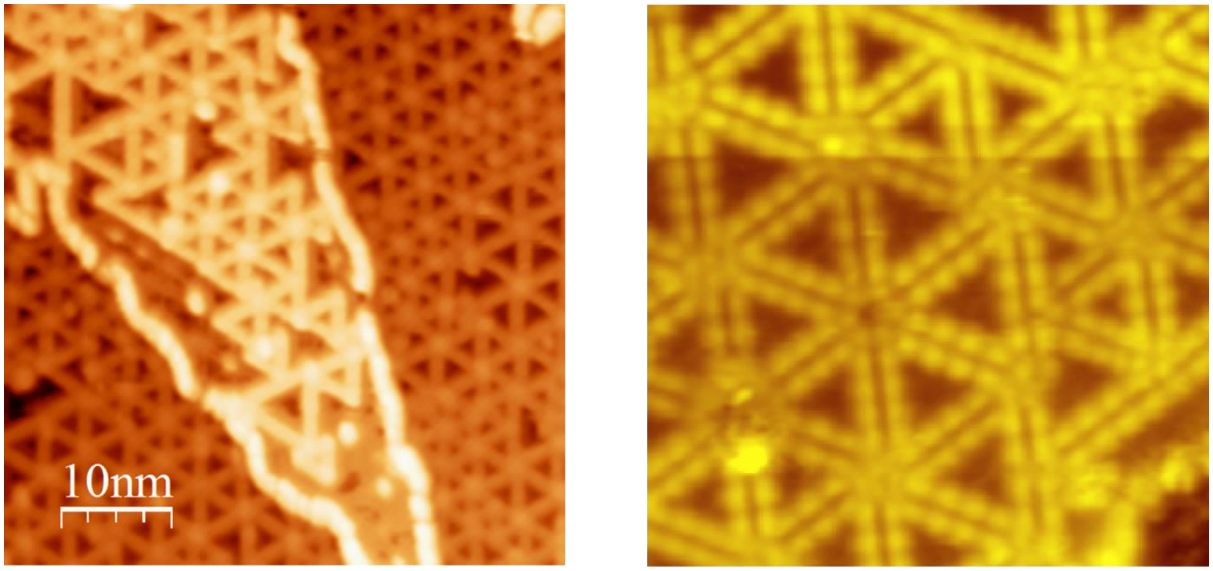

Figure 5 (a) STEM micrograph showing the IDB defect (boxed by the red thin line) in ML $MoSe_2$. The green and pink dots mark Se and Mo atoms, respectively. (b) Top- and side-views of a stick-and-ball model of the IDB defects in $MoSe_2$ [50].

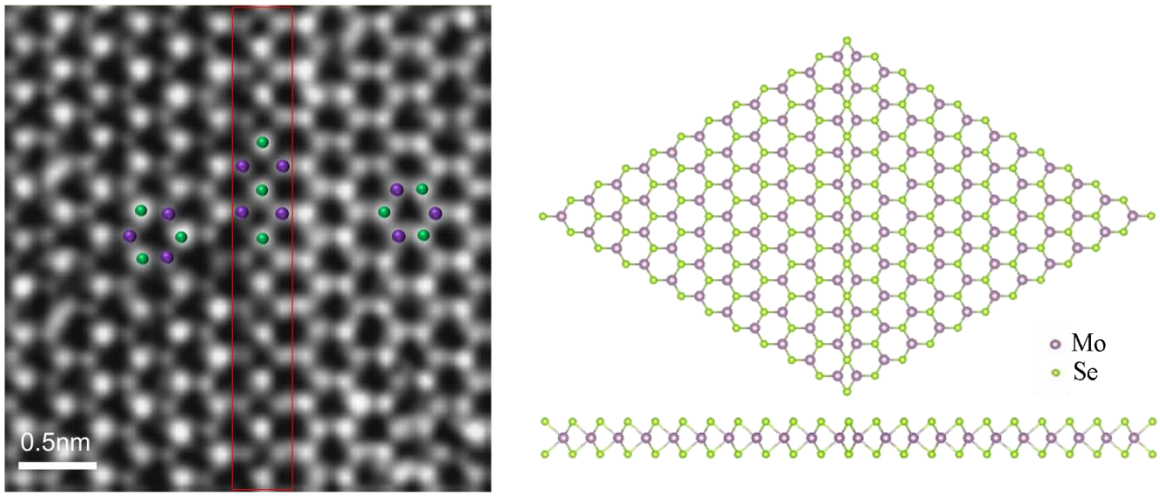

(a) (b)

Figure 6 (a) Energy and wave-vector ($k \sim 2\pi/\lambda$) relation derived from STS maps for the IDB defects with different lengths (coded by different colours). The inset shows the derivation of k (or λ) by fitting of the intensity undulation by the squared sinusoidal function. (b, c) Examples of the STS maps (size: 4.5×4.5 nm^2) at different energies as marked. Reprinted with permission from ref. [27]. Copyright (2014) by the American Physical Society.

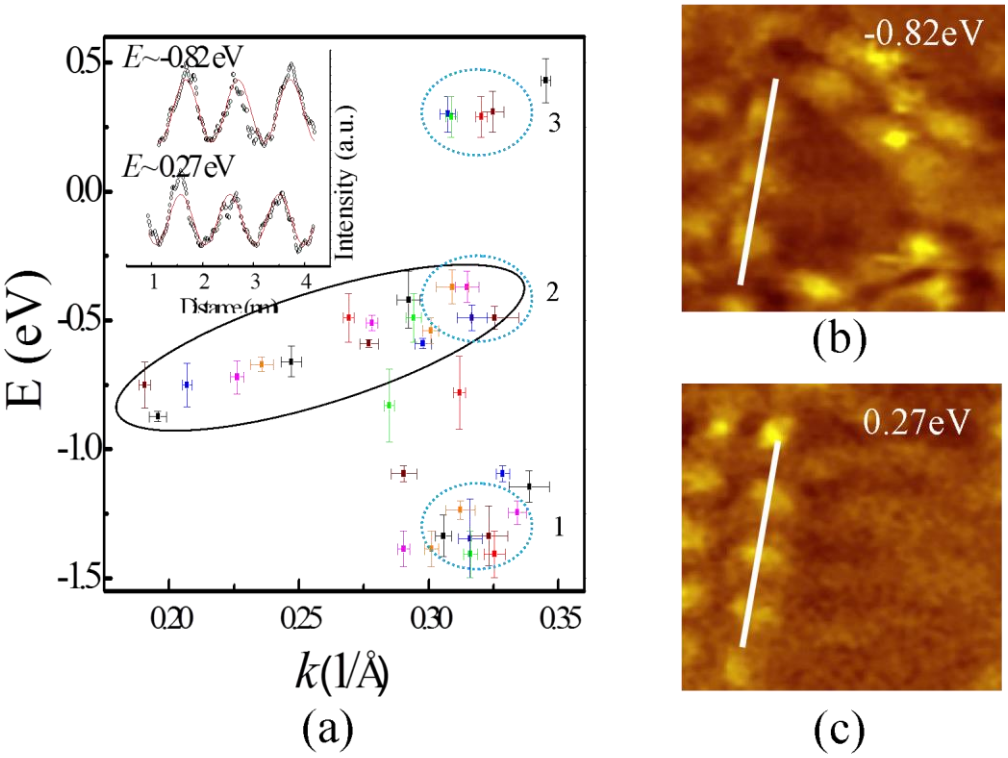

Figure 7 STM images of monolayer $MoTe_2$ of the same area (size: 8×8 nm^2) but with different bias conditions: (a) 2.0 V, (b) 0.80 V, and (c) 0.40 V. (d) A STM micrograph (size: 8×8 nm^2, bias: 0.80 V) of the same sample but at a different location. The two highlighted triangles of different sizes contain different undulation patterns. (b)-(d) Reprinted with permission from Ref. [31]. Copyright (2017) by the American Chemical Society.

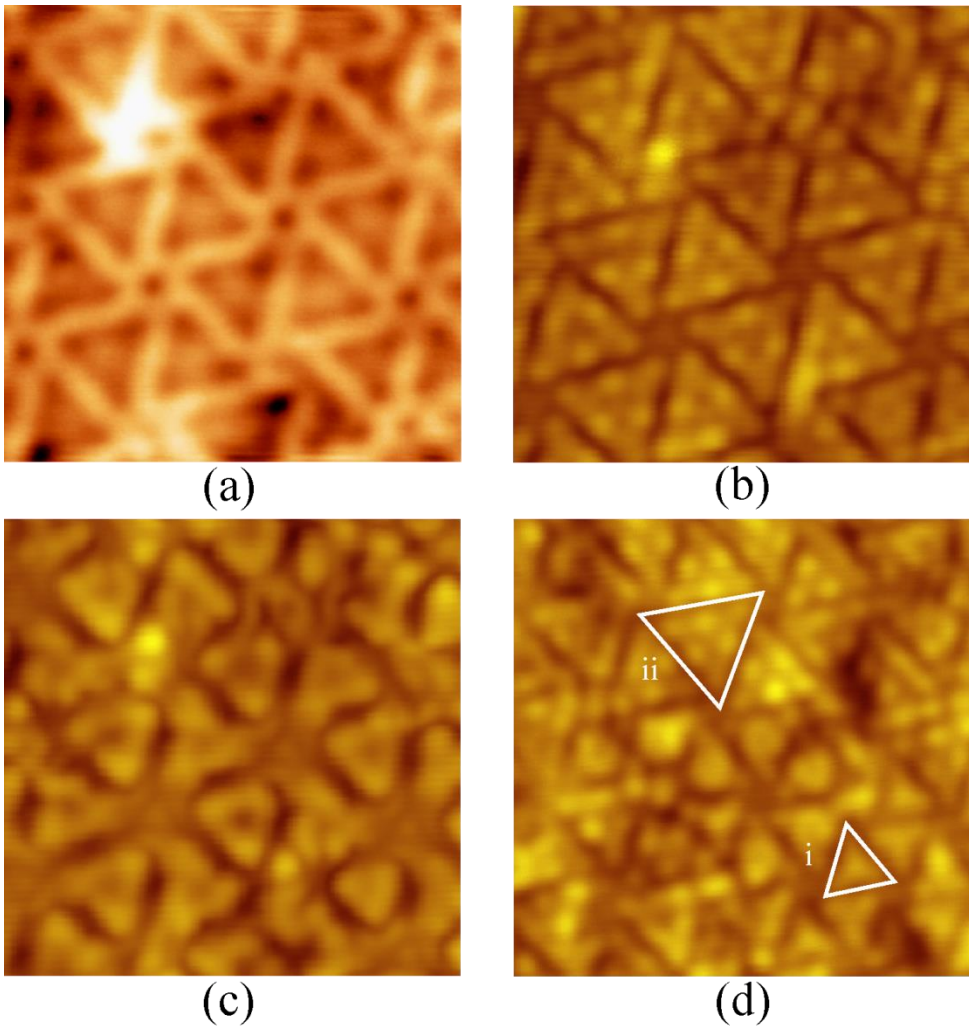

Figure 8 (a) STS map (size: 9×9 nm^2, bias: 0.56 V) of a BL $MoSe_2$ showing an elliptical ionization ring (highlighted by the red circle). (b) Position dependent dI/dV spectra revealing the variation of the ring size with energy. The black line represents a simulation result assuming the ionization energy of 0.24 eV and effective dielectric constant of 4.6. Reprinted with permission from ref. [29]. Copyright (2015) by the American Chemical Society.

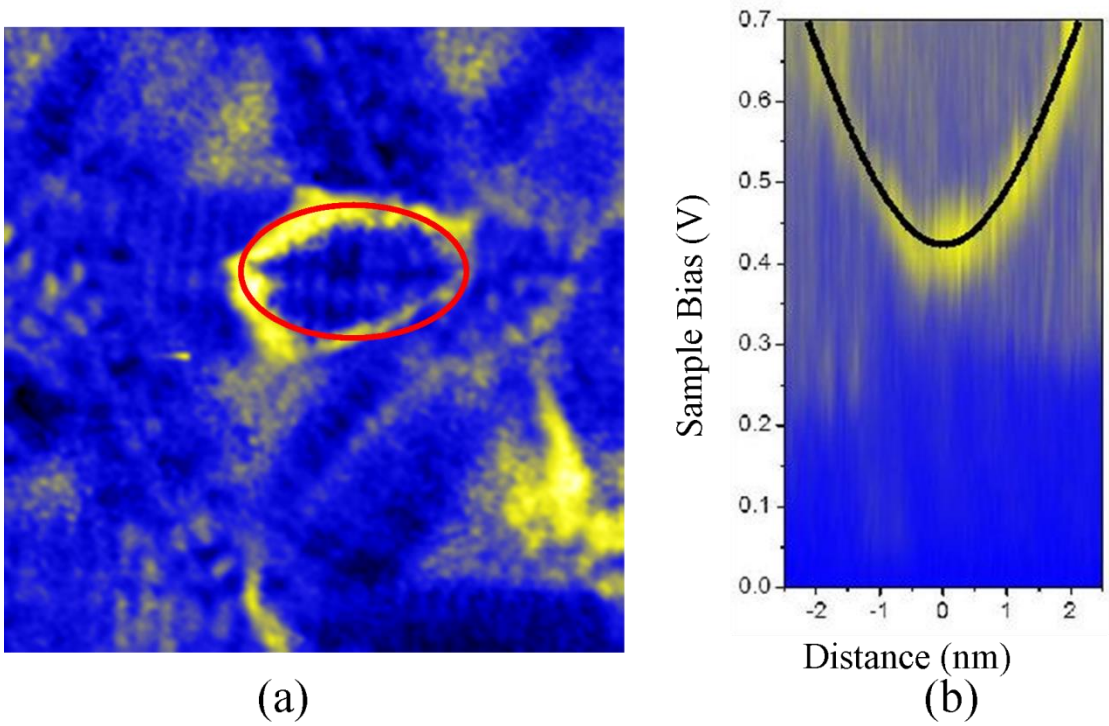

Figure 9 (a) A STS map (size: 10×10 nm^2, bias: 1.0V) of ML WSe_2 containing two point defects, revealing the QPI pattern. (b) Fast Fourier Transform of the STS map. (c) A constant energy contour map at the corresponding energy of the experiment, in which the solid green arrows mark possible spin-conserving intervalley scattering events. (d) Calculated joint density of states for spin-conserving scattering at the energy close to the CBM [28].

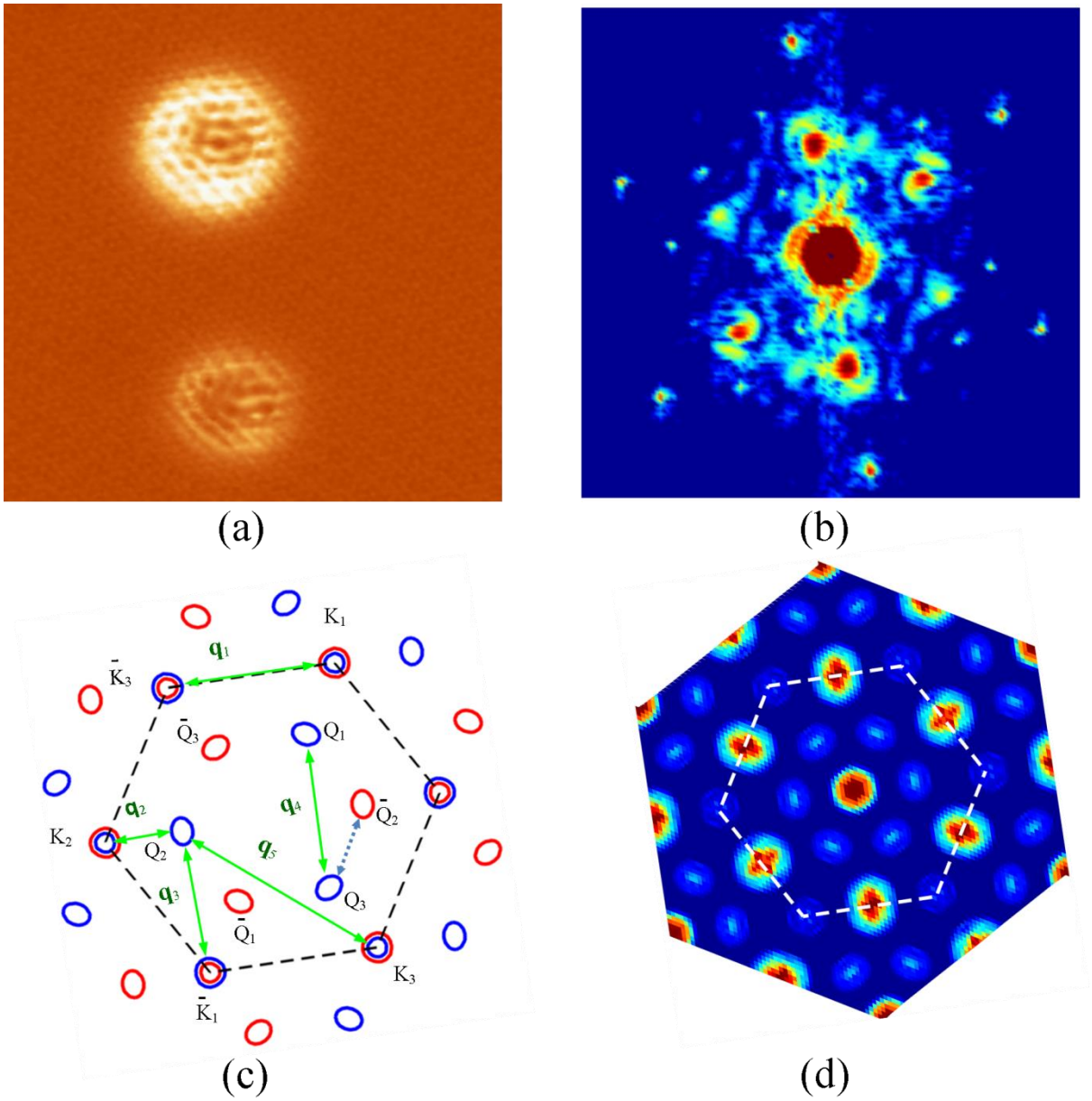

Figure 10 (a) STM image (size: 50×50 nm^2, bias: 0.5V) of as-grown $MoTe_2$ sample of submonolayer coverage. The inset is a line profile taken along the white line revealing monolayer $MoTe_2$ islands. (b, c) Atomic resolution STM images of 2H (b) and 1T' (c) phase $MoTe_2$ as illustrated by the stick-and-ball models shown in the inset. Reprinted with permission from Ref. [31]. Copyright (2017) by the American Chemical Society.

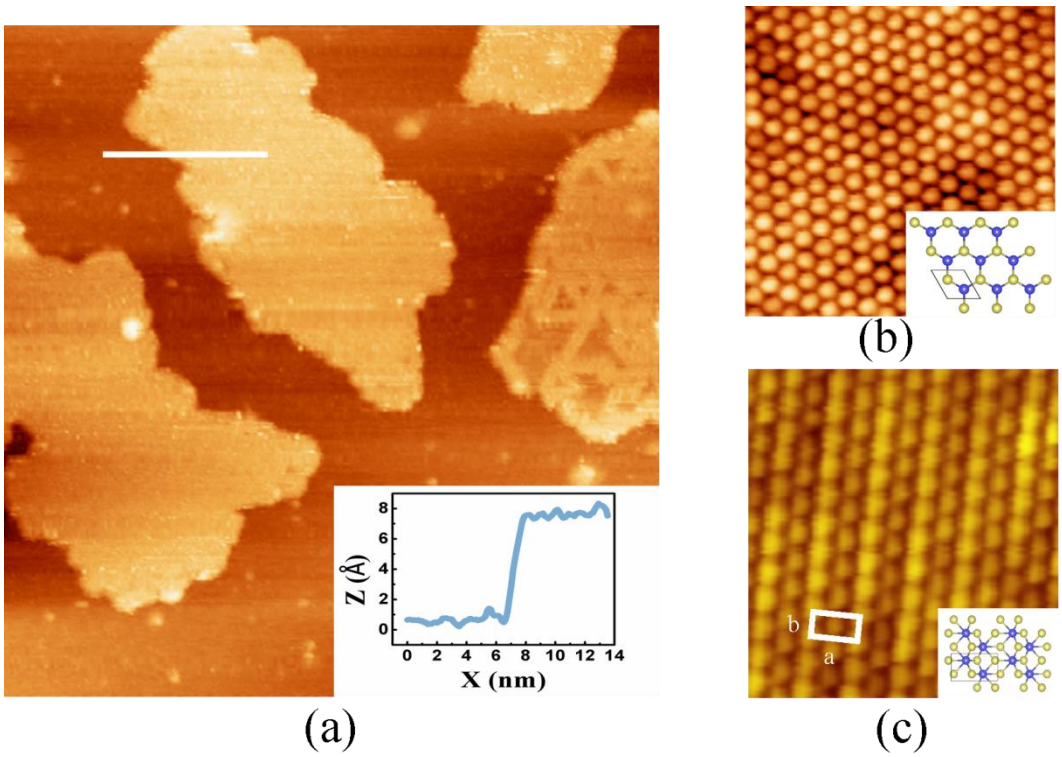

Figure 11 (a) RHEED pattern of as as-grown $MoTe_2$ showing two sets of diffraction streaks corresponding to the 2H and 1T' phases as indicated by the arrows shown on top. (b, c) Ratio *R* of the 1T'-streak intensity with that of the sum of 1T' and 2H-streaks as a function of deposition temperature (b) and Te flux (c). Reprinted with permission from Ref. [31]. Copyright (2017) by the American Chemical Society.

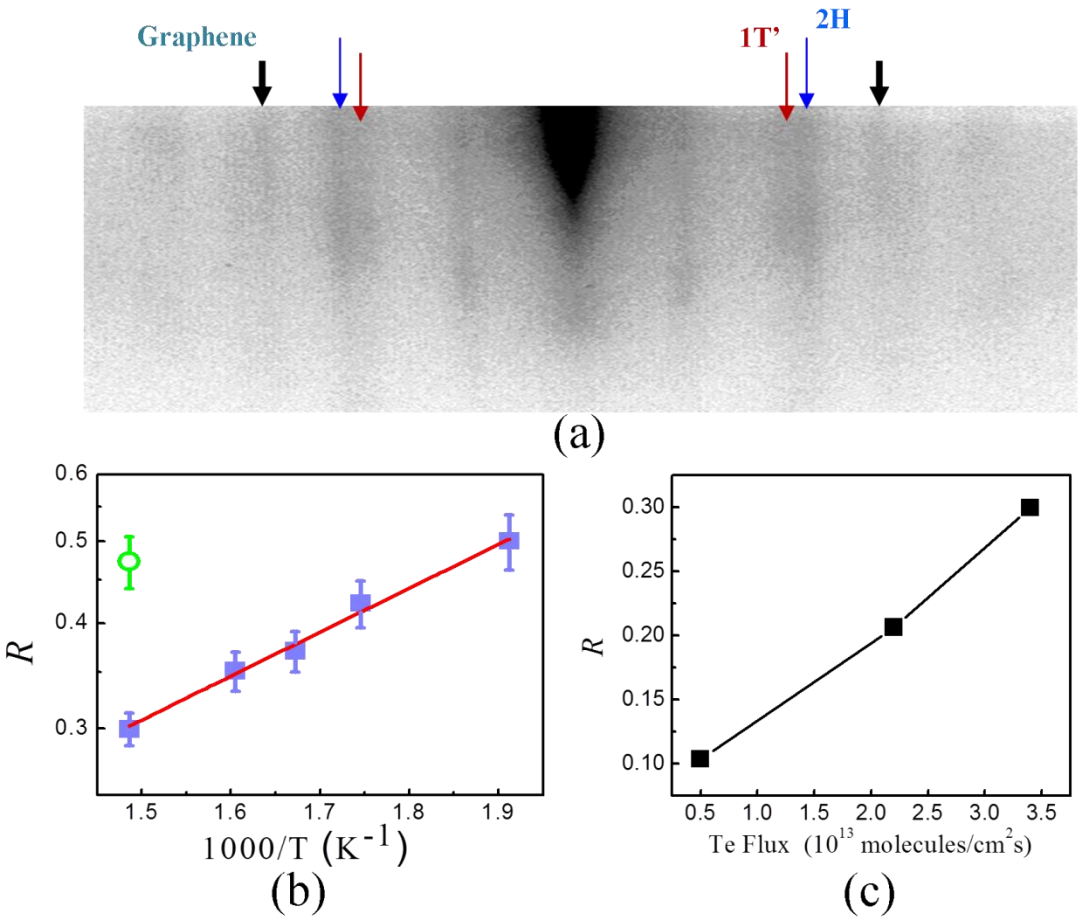

Figure 12 (a) STS map (size: 8×4 nm^2, bias: 0.5 V) of the 1T'-$MoTe_2$ close to the domain boundary showing quasi-periodic bright bands. (b) Fast Fourier Transform of (a) showing quasi-particle interference pattern. (c) Constant energy contour map at the corresponding energy illustrating an intervalley scattering event (green arrow) that can lead to such QPI. Reprinted with permission from Ref. [31]. Copyright (2017) by the American Chemical Society.

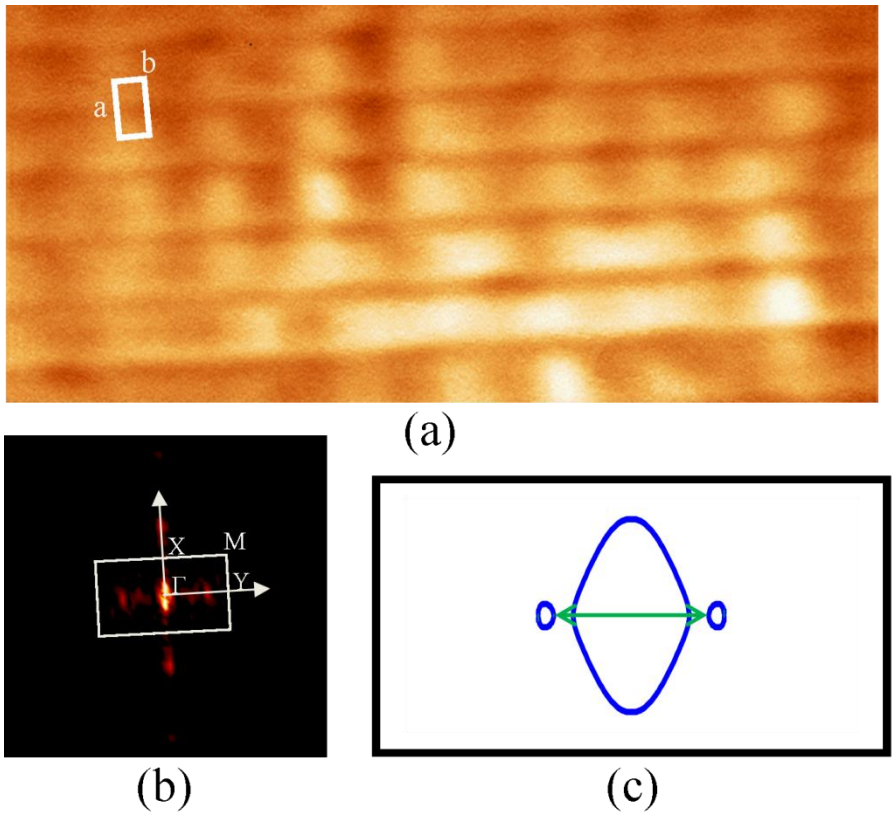

References

[1] K. F. Mak, C. Lee, J. Hone, J. Shan, and T. F. Heinz, *Phys Rev Lett* **105** (2010) 136805.
[2] A. Splendiani, L. Sun, Y. Zhang, T. Li, J. Kim, C. Y. Chim, G. Galli, and F. Wang, *Nano Lett* **10** (2010) 1271.
[3] T. Cheiwchanchamnangij and W. R. L. Lambrecht, *Phys Rev B* **85** (2012).
[4] D. Y. Qiu, H. Felipe, and S. G. Louie, *Phys Rev Lett* **111** (2013) 216805.
[5] Z. Ye, T. Cao, K. O'Brien, H. Zhu, X. Yin, Y. Wang, S. G. Louie, and X. Zhang, *Nature* **513** (2014) 214.
[6] K. He, N. Kumar, L. Zhao, Z. Wang, K. F. Mak, H. Zhao, and J. Shan, *Phys Rev Lett* **113** (2014) 026803.
[7] A. Chernikov, T. C. Berkelbach, H. M. Hill, A. Rigosi, Y. Li, O. B. Aslan, D. R. Reichman, M. S. Hybertsen, and T. F. Heinz, *Phys Rev Lett* **113** (2014) 076802.
[8] S. Najmaei, Z. Liu, W. Zhou, X. Zou, G. Shi, S. Lei, B. I. Yakobson, J. C. Idrobo, P. M. Ajayan, and J. Lou, *Nat Mater* **12** (2013) 754.
[9] C. Zhang, A. Johnson, C.-L. Hsu, L.-J. Li, and C.-K. Shih, *Nano Lett* **14** (2014) 2443.
[10] M. M. Ugeda, A. J. Bradley, S.-F. Shi, H. Felipe, Y. Zhang, D. Y. Qiu, W. Ruan, S.-K. Mo, Z. Hussain, and Z.-X. Shen, *Nat Mater* **13** (2014) 1091.
[11] A. Hanbicki, M. Currie, G. Kioseoglou, A. Friedman, and B. Jonker, *Solid State Commun* **203** (2015) 16.
[12] D. Xiao, G.-B. Liu, W. Feng, X. Xu, and W. Yao, *Phys Rev Lett* **108** (2012) 196802.
[13] Z. Zhu, Y. Cheng, and U. Schwingenschlögl, *Phys Rev B* **84** (2011) 153402.
[14] A. Rycerz, J. Tworzydło, and C. Beenakker, *Nat Phys* **3** (2007) 172.
[15] D. Xiao, W. Yao, and Q. Niu, *Phys Rev Lett* **99** (2007) 236809.
[16] G.-B. Liu, D. Xiao, Y. Yao, X. Xu, and W. Yao, *Chem Soc Rev* **44** (2015) 2643.
[17] X. Xu, W. Yao, D. Xiao, and T. F. Heinz, *Nat Phys* **10** (2014) 343.
[18] Q. H. Wang, K. Kalantar-Zadeh, A. Kis, J. N. Coleman, and M. S. Strano, *Nat Nanotechnol* **7** (2012) 699.
[19] K. S. Novoselov, D. Jiang, F. Schedin, T. J. Booth, V. V. Khotkevich, S. V. Morozov, and A. K. Geim, *Proc Natl Acad Sci U S A* **102** (2005) 10451.
[20] Y. H. Lee, X. Q. Zhang, W. Zhang, M. T. Chang, C. T. Lin, K. D. Chang, Y. C. Yu, J. T. Wang, C. S. Chang, L. J. Li, and T. W. Lin, *Adv Mater* **24** (2012) 2320.
[21] A. M. van der Zande, P. Y. Huang, D. A. Chenet, T. C. Berkelbach, Y. You, G. H. Lee, T. F. Heinz, D. R. Reichman, D. A. Muller, and J. C. Hone, *Nat Mater* **12** (2013) 554.
[22] S. Wu, C. Huang, G. Aivazian, J. S. Ross, D. H. Cobden, and X. Xu, *ACS nano* **7** (2013) 2768.
[23] C. Zhang, Y. Chen, A. Johnson, M. Y. Li, L. J. Li, P. C. Mende, R. M. Feenstra, and C. K. Shih, *Nano Lett* **15** (2015) 6494.
[24] C. Zhang, Y. Chen, J. K. Huang, X. Wu, L. J. Li, W. Yao, J. Tersoff, and C. K. Shih, *Nat Commun* **6** (2016) 10349.
[25] M. M. Ugeda, A. J. Bradley, S. F. Shi, F. H. da Jornada, Y. Zhang, D. Y. Qiu, W. Ruan, S. K. Mo, Z. Hussain, Z. X. Shen, F. Wang, S. G. Louie, and M. F. Crommie, *Nat Mater* **13** (2014) 1091.
[26] A. J. Bradley, M. U. M, F. H. da Jornada, D. Y. Qiu, W. Ruan, Y. Zhang, S. Wickenburg, A. Riss, J. Lu, S. K. Mo, Z. Hussain, Z. X. Shen, S. G. Louie, and M. F. Crommie, *Nano Lett* **15** (2015) 2594.
[27] H. Liu, L. Jiao, F. Yang, Y. Cai, X. Wu, W. Ho, C. Gao, J. Jia, N. Wang, and H. Fan, *Phys Rev Lett* **113** (2014) 066105.
[28] H. Liu, J. Chen, H. Yu, F. Yang, L. Jiao, G. B. Liu, W. Ho, C. Gao, J. Jia, W. Yao, and M. Xie, *Nat Commun* **6** (2015) 8180.
[29] H. Liu, H. Zheng, F. Yang, L. Jiao, J. Chen, W. Ho, C. Gao, J. Jia, and M. Xie, *ACS nano* **9** (2015) 6619.
[30] L. Jiao, H. J. Liu, J. L. Chen, Y. Yi, W. G. Chen, Y. Cai, J. N. Wang, X. Q. Dai, N. Wang, W. K. Ho, and M. H. Xie, *New J Phys* **17** (2015) 053023.
[31] J. Chen, G. Wang, Y. Tang, H. Tian, J. Xu, X. Dai, H. Xu, J. Jia, W. Ho, and M. Xie, *ACS nano* **11** (2017) 3282.

[32] H. Liu, L. Jiao, L. Xie, F. Yang, J. Chen, W. Ho, C. Gao, J. Jia, X. Cui, and M. Xie, *2d Mater* **2** (2015) 034004.
[33] R. V. Coleman, B. Drake, P. K. Hansma, and G. Slough, *Phys Rev Lett* **55** (1985) 394.
[34] T. Mori, K. Saiki, and A. Koma, *Jpn J Appl Phys* **31** (1992) L1370.
[35] R. Coehoorn, C. Haas, and R. De Groot, *Phys Rev B* **35** (1987) 6203.
[36] G. B. Liu, D. Xiao, Y. Yao, X. Xu, and W. Yao, *Chem Soc Rev* (2014).
[37] F. S. Ohuchi, B. A. Parkinson, K. Ueno, and A. Koma, *J Appl Phys* **68** (1990) 2168.
[38] A. Koma, *J Cryst Growth* **201** (1999) 236.
[39] F. Ohuchi, T. Shimada, B. Parkinson, K. Ueno, and A. Koma, *J Cryst Growth* **111** (1991) 1033.
[40] H. Li, Z. Wang, X. Kan, X. Guo, H. He, Z. Wang, J. Wang, T. Wong, N. Wang, and M. H. Xie, *New J Phys* **12** (2010) 103038.
[41] K. Ueno, M. Sakurai, and A. Koma, *J Cryst Growth* **150** (1995) 1180.
[42] K.-Y. Liu, K. Ueno, Y. Fujikawa, K. Saiki, and A. Koma, *Jpn J Appl Phys* **32** (1993) L434.
[43] J. Tersoff and D. Hamann, *Phys Rev Lett* **50** (1983) 1998.
[44] J. Tersoff and D. R. Hamann, *Phys Rev B* **31** (1985) 805.
[45] M. V. Bollinger, J. V. Lauritsen, K. W. Jacobsen, J. K. Norskov, S. Helveg, and F. Besenbacher, *Phys Rev Lett* **87** (2001) 196803.
[46] H. Murata and A. Koma, *Phys Rev B* **59** (1999) 10327.
[47] S. Barja, S. Wickenburg, Z.-F. Liu, Y. Zhang, H. Ryu, M. M. Ugeda, Z. Hussain, Z.-X. Shen, S.-K. Mo, and E. Wong, *Nat Phys* **12** (2016) 751.
[48] Y. Ma, S. Kolekar, H. Coy Diaz, J. Aprojanz, I. Miccoli, C. Tegenkamp, and M. Batzill, *ACS nano* **11** (2017) 5130.
[49] Y. Ma, H. C. Diaz, J. Avila, C. Chen, V. Kalappattil, R. Das, M. H. Phan, T. Cadez, J. M. Carmelo, M. C. Asensio, and M. Batzill, *Nat Commun* **8** (2017) 14231.
[50] J. Hong and C. Jin, *unpublished* (2017).
[51] C. Segarra, J. Planelles, and S. E. Ulloa, *Phys Rev B* **93** (2016).
[52] K. Teichmann, M. Wenderoth, S. Loth, R. Ulbrich, J. Garleff, A. Wijnheijmer, and P. Koenraad, *Phys Rev Lett* **101** (2008) 076103.
[53] H. Zheng, J. Kröger, and R. Berndt, *Phys Rev Lett* **108** (2012) 076801.
[54] D.-H. Lee and J. A. Gupta, *Nano Lett* **11** (2011) 2004.
[55] C.-L. Song, B. Sun, Y.-L. Wang, Y.-P. Jiang, L. Wang, K. He, X. Chen, P. Zhang, X.-C. Ma, and Q.-K. Xue, *Phys Rev Lett* **108** (2012) 156803.
[56] M. N. Ali, J. Xiong, S. Flynn, J. Tao, Q. D. Gibson, L. M. Schoop, T. Liang, N. Haldolaarachchige, M. Hirschberger, N. P. Ong, and R. J. Cava, *Nature* **514** (2014) 205.
[57] I. Pletikosić, M. N. Ali, A. V. Fedorov, R. J. Cava, and T. Valla, *Phys Rev Lett* **113** (2014).
[58] J. Jiang, F. Tang, X. Pan, H. Liu, X. Niu, Y. Wang, D. Xu, H. Yang, B. Xie, and F. Song, *Phys Rev Lett* **115** (2015) 166601.
[59] Y. Luo, H. Li, Y. M. Dai, H. Miao, Y. G. Shi, H. Ding, A. J. Taylor, D. A. Yarotski, R. P. Prasankumar, and J. D. Thompson, *Appl Phys Lett* **107** (2015) 182411.
[60] H. Y. Lv, W. J. Lu, D. F. Shao, Y. Liu, S. G. Tan, and Y. P. Sun, *Europhys Lett* **110** (2015) 37004.
[61] D. Rhodes, S. Das, Q. R. Zhang, B. Zeng, N. R. Pradhan, N. Kikugawa, E. Manousakis, and L. Balicas, *Phys Rev B* **92** (2015).
[62] D. H. Keum, S. Cho, J. H. Kim, D.-H. Choe, H.-J. Sung, M. Kan, H. Kang, J.-Y. Hwang, S. W. Kim, H. Yang, K. J. Chang, and Y. H. Lee, *Nat Phys* **11** (2015) 482.
[63] J. L. Xiaofeng Qian, Liang Fu, Ju Li, *Science* **346** (2014).
[64] Z. Fei, T. Palomaki, S. Wu, W. Zhao, X. Cai, B. Sun, P. Nguyen, J. Finney, X. Xu, and D. H. Cobden, *Nat Phys* **13** (2017) 677.
[65] S. Tang, C. Zhang, D. Wong, Z. Pedramrazi, H.-Z. Tsai, C. Jia, B. Moritz, M. Claassen, H. Ryu, S. Kahn, J. Jiang, H. Yan, M. Hashimoto, D. Lu, R. G. Moore, C.-C. Hwang, C. Hwang, Z. Hussain, Y. Chen, M. M. Ugeda, Z. Liu, X. Xie, T. P. Devereaux, M. F. Crommie, S.-K. Mo, and Z.-X. Shen, *Nat Phys* **13** (2017) 683.
[66] A. A. Soluyanov, D. Gresch, Z. Wang, Q. Wu, M. Troyer, X. Dai, and B. A. Bernevig, *Nature* **527** (2015) 495.

[67] K. Deng, G. Wan, P. Deng, K. Zhang, S. Ding, E. Wang, M. Yan, H. Huang, H. Zhang, Z. Xu, J. Denlinger, A. Fedorov, H. Yang, W. Duan, H. Yao, Y. Wu, S. Fan, H. Zhang, X. Chen, and S. Zhou, *Nat Phys* (2016).
[68] C. Wang, Y. Zhang, J. Huang, S. Nie, G. Liu, A. Liang, Y. Zhang, B. Shen, J. Liu, C. Hu, Y. Ding, D. Liu, Y. Hu, S. He, L. Zhao, L. Yu, J. Hu, J. Wei, Z. Mao, Y. Shi, X. Jia, F. Zhang, S. Zhang, F. Yang, Z. Wang, Q. Peng, H. Weng, X. Dai, Z. Fang, Z. Xu, C. Chen, and X. J. Zhou, *Phys Rev B* **94** (2016).
[69] J. Jiang, Z. K. Liu, Y. Sun, H. F. Yang, C. R. Rajamathi, Y. P. Qi, L. X. Yang, C. Chen, H. Peng, C. C. Hwang, S. Z. Sun, S. K. Mo, I. Vobornik, J. Fujii, S. S. Parkin, C. Felser, B. H. Yan, and Y. L. Chen, *Nat Commun* **8** (2017) 13973.
[70] T. R. Chang, S. Y. Xu, G. Chang, C. C. Lee, S. M. Huang, B. Wang, G. Bian, H. Zheng, D. S. Sanchez, I. Belopolski, N. Alidoust, M. Neupane, A. Bansil, H. T. Jeng, H. Lin, and M. Zahid Hasan, *Nat Commun* **7** (2016) 10639.